



# Nonlinear coupling between occipital and motor cortex during motor imagery: A dynamic causal modeling study

B.C.M. van Wijk<sup>a,\*</sup>, V. Litvak<sup>b</sup>, K.J. Friston<sup>b</sup>, A. Daffertshofer<sup>a</sup>

<sup>a</sup> Research Institute MOVE, VU University Amsterdam, Amsterdam, The Netherlands

<sup>b</sup> Wellcome Trust Centre for Neuroimaging, UCL Institute of Neurology, London, UK

## ARTICLE INFO

### Article history:

Accepted 31 December 2012

Available online 11 January 2013

### Keywords:

Cross-frequency coupling

Dynamic causal modeling

Effective connectivity

Induced responses

MEG

Motor imagery

## ABSTRACT

We demonstrate the capacity of dynamic causal modeling to characterize the nonlinear coupling among cortical sources that underlie time–frequency modulations in MEG data. Our experimental task involved the mental rotation of hand drawings that ten subjects used to decide if it was a right or left hand. Reaction times were shorter when the stimuli were presented with a small rotation angle (fast responses) compared to a large rotation angle (slow responses). The grand-averaged data showed that in both cases performance was accompanied by a marked increase in gamma activity in occipital areas and a concomitant decrease in alpha and beta power in occipital and motor regions. Modeling directed (cross) frequency interactions between the two regions revealed that after the stimulus induced a gamma increase and beta decrease in occipital regions, interactions with the motor area served to attenuate these modulations. The difference between fast and slow behavioral responses was manifest as an altered coupling strength in both forward and backward connections, which led to a less pronounced attenuation for more difficult (slow reaction time) trials. This was mediated by a (backwards) beta to gamma coupling from motor till occipital sources, whereas other interactions were mainly within the same frequency. Results are consistent with the theory of predictive coding and suggest that during motor imagery, the influence of motor areas on activity in occipital cortex co-determines performance. Our study illustrates the benefit of modeling experimental responses in terms of a generative model that can disentangle the contributions of intra-areal vis-à-vis inter-areal connections to time–frequency modulations during task performance.

© 2013 Elsevier Inc. All rights reserved.

## Introduction

Studying task-dependent communication between brain regions is essential to link behavior with its accompanying neural activity. Using non-invasive recording techniques like M/EEG recordings one can characterize distinct rhythmic activities that differ with region and modulate with task. To estimate the coupling strength between regions or sources, most studies concentrate on iso-frequency connections, which are relatively easy to address and to interpret. For example, cross-regional information transfer can be treated by assuming a simple linear response system and connectivity can be determined through standard regression techniques. However, by definition, these approaches are blind to cross-frequency interactions. Moreover, directionality of connections is often ignored although it is

considered important, if not essential, for neural functioning. Recent advances that address directionality in the analysis of M/EEG data include, e.g., Granger causality, the directed transfer function, and the phase slope index (Nolte et al., 2008). Likewise the introduction of generalized phase coupling (Tass et al., 1998), and empirical findings of cross-frequency phase–amplitude (Canolty and Knight, 2010; Jensen and Colgin, 2007), and amplitude–amplitude correlations (Bruns and Eckhorn, 2004; de Lange et al., 2008), underscore the relevance of multi-frequency coupling for neural functioning.

Alternatively, one might follow a slightly different route by first formalizing explicit models that are supposed to generate empirically observed neural activity and use the structure and parameters of these models to infer effective connectivity in a (small) network of regions. In doing so, knowledge about neuroanatomy and the neurophysiological processes at work can be incorporated. Fitting the model to observed data gives an estimate of its parameters that quantify the coupling strength within and between regions. This is standard procedure in the vast field of system identification and forms the rationale behind dynamic causal modeling (DCM); where different configurations of sources and their connections are tested to find the most likely network generating observed task-related responses.

\* Corresponding author at: Faculty of Human Movement Sciences, VU University Amsterdam, Van der Boerhorststraat 9, 1081 BT Amsterdam, The Netherlands. Fax: +31 20 59 88529.

E-mail address: [vanwijk.bernadette@gmail.com](mailto:vanwijk.bernadette@gmail.com) (B.C.M. van Wijk).

DCM was initially developed for the analysis of fMRI data (Friston et al., 2003) that – to a good approximation – can be modeled with first-order, linear differential neuronal state equations, and more detailed hemodynamic response functions. In more recent work this approach has been extended to model evoked responses in both EEG and MEG (David et al., 2006). Due to high temporal resolution of M/EEG recordings, the neural state equations are replaced by neurophysiologically more realistic, neural mass models based on studies by Jansen and Rit (1995). Subsequently, DCM has been adjusted to other data features: cross-spectral densities underlying steady state-responses (Moran et al., 2009), complex-valued cross-spectral densities (Friston et al., 2012), time-resolved modulations of spectral power (Chen et al., 2008), and synchronization by means of phase coupling (Penny et al., 2009).

Here, we demonstrate the capacity of DCM to investigate time–frequency modulations in visual and motor areas during motor imagery. The experimental task under study involved the mental rotation of hand drawings as described by de Lange et al. (2008). Subjects used mental rotation in order to report whether the drawing contained a left or right hand. Reaction times typically increased when the images were shown with a larger rotation angle. Executing the task induced a strong increase in gamma activity over visual areas, and a decrease in alpha and beta activity in both visual and motor areas. de Lange et al. (2008) also found a negative correlation between occipital gamma and beta activity in the motor cortex that became stronger over time after stimulus onset and dissolved just before response onset. To disentangle directional cross-frequency couplings underlying these time–frequency modulations, we employed DCM and contrasted trials with short and long reaction times. Do trials with fast and slow reaction times differ in time–frequency modulations after stimulus presentation, and if so, are slow reaction times associated with altered forward (from visual to motor cortex) and/or backward (from motor to visual cortex) information processing?

## Methods

### Behavioral task and recordings

de Lange et al. (2008) have described the experiment in detail. Briefly, twelve subjects performed a motor imagery task in which they needed to identify line drawings of a human hand as a left or right hand. The drawings were presented with five different rotation angles between 40 and 180°. Each trial started with a 3 s baseline period, after which a drawing of a hand was presented. The task required mental rotation of the hand drawing, since subjects were instructed to respond as fast as possible after recognizing the laterality of the hand by pressing one of two buttons with the right hand. The hand was presented either with the palm or the back facing forward and was displayed until a response was given. In total, 800 trials were performed in a random order. Brain activity was recorded using a 151-channel CTF MEG system. Data were sampled at a rate of 1200 Hz after online low-pass-filtering with 300 Hz. The electro-oculogram was co-recorded to identify trials with excessive eye movements and trials containing artifacts were discarded offline. Head position was localized at the start and end of the recording session, using coils on the nasion and pre-auricular points. In addition, individual structural MRI scans were obtained. Here we re-analyzed the data from the original paper using Matlab (version R2007b, MathWorks, Natwick, MA) and SPM8 (Update revision number 4667, <http://www.fil.ion.ucl.ac.uk/spm>, Litvak et al., 2011).

### Source localization

de Lange et al. (2008) found an increase in gamma activity (50–80 Hz) over occipital areas peaking shortly after stimulus onset, and a sustained decrease in beta activity (16–24 Hz) over occipital/

parietal and motor areas before response onset. To localize the origin of these modulations, we used a linearly constrained minimum variance beamformer (Hillebrand and Barnes, 2005). For the gamma band we selected the time interval between 100 and 600 ms after stimulus onset (at 0 ms) and for the beta band the time interval –700 to –200 ms before response onset. The localized power in these intervals was contrasted against that during the –500 to 0 ms pre-stimulus baseline interval. The beamformer grid resolution was set to  $10 \times 10 \times 10$  mm using the individual MRI scans. To allow post-hoc averaging over subjects (see below) the individual beamformer images were transformed to template space. Values on the grid were then interpolated using linear interpolation to produce volumetric images with 2 mm resolution (without further smoothing). The resulting images of source power differences between active and baseline intervals were averaged over subjects. We found large power differences in left and right visual cortex (from here on referred to as ‘O’ for occipital) as well as sources in left and right sensorimotor cortex (referred to as ‘M’ for motor). See Fig. 1 for their specific locations. In addition, left and right parietal sources could be discerned, which revealed time–frequency spectra that closely resembled that of the sources in sensorimotor areas. Given the similarity between parietal and motor responses, we focused on the motor regions in subsequent DCM analyses. Locations of the sources in individual subjects were identified as the closest to the mean peak location over subjects. For one subject no clear right O source could be identified. Likewise, for three subjects no right M source could be detected. In these cases, unilateral sources were used for subsequent analyses. Finally, source time series were extracted for all selected trials using beamformer weights that were

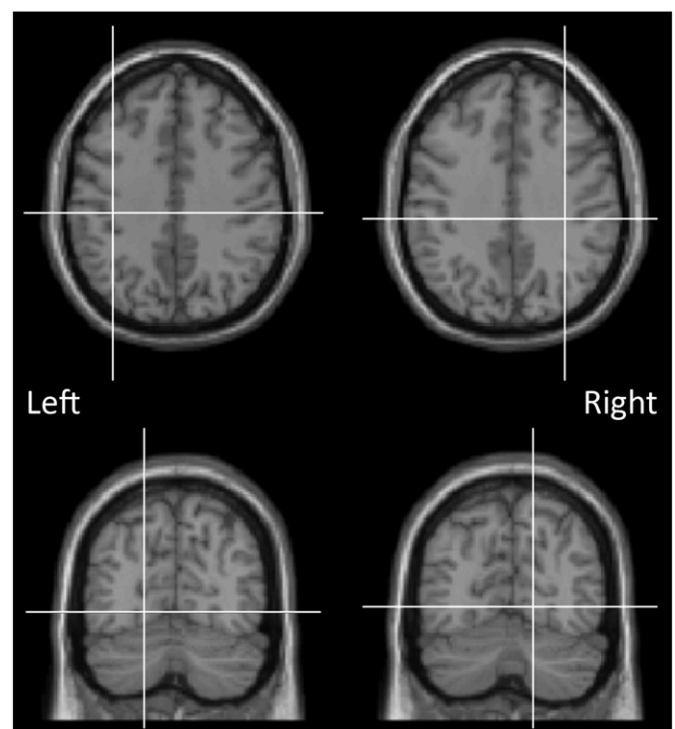


**Fig. 1.** Source locations used for DCM. The crosshairs indicate the peak locations of the grand-averaged power contrast images. Top row: beta band (16–24 Hz) decrease in M [left:  $-37 - 25 - 39$  mm; right:  $34 - 28 - 37$  mm]. Bottom row: gamma band (50–80 Hz) increase in O [left:  $-18 - 71 - 5$  mm; right:  $14 - 69 - 2$  mm]. Sources in individual subjects were identified as the closest to these locations (mean Euclidean distance from the grand-averaged peak locations: left M: 15 mm; right M: 18 mm; left O: 14 mm; right O: 13 mm).

recalculated for all frequencies and were treated as samples from virtual (intracranial) electrodes.

### Trial selection

Longer reaction times were found for hand drawings presented with larger rotation angles. As a result, reaction times for all trials together showed considerable variation both between and within subjects. To ensure typical neuronal responses during stimulus processing with the same time course of time–frequency modulations, all trials with a reaction time within a 200 ms interval (separately for fast and slow reaction trials) were selected for further processing. By the same token, a sufficient number of trials had to be available for rendering spectral estimates reliable. We chose a reaction time interval between 800 and 1000 ms for short reaction time trials and 1200 to 1400 ms for long reaction time trials. To guarantee that no differences in signal-to-noise ratios occurred due to a mismatch in the number of trials for the two types of trial within a subject, the same number of trials was chosen for both intervals by discarding excess trials in the interval with the largest number of trials. For two subjects there were less than forty trials and their data were excluded from further analysis. For the remaining ten subjects a suitable number of trials were analyzed (# trials = 40, 44, 51, 51, 65, 68, 70, 90, 102, 105).

### Time–frequency spectra

The grand-averaged time–frequency spectra (over 900 ms) of induced power in O and M (time locked to stimulus onset) served as the observed data that was explained with DCM. First, the induced power for each subject and source was calculated using the selected trials. For this averaging, the average over trials in the time-domain was subtracted from each trial, prior to transforming to the frequency domain. Time–frequency spectra were estimated using Morlet wavelets with a width of five periods, using frequencies ranging from 9 to 99 Hz with a step size of 2 Hz. The time window started 300 ms before stimulus onset and lasted until 600 ms after stimulus onset (for both short and long reaction time trials) to avoid response-related activity in the short reaction time trials. Prior to averaging over trials, the time–frequency spectra were log-transformed and normalized by subtracting for each frequency the average log power in the baseline interval (−300 to 0 ms). As left and right hand trials yielded very similar (often bilateral) results, the spectra were averaged over all trials and over left and right sources of O and M (when detectable) to improve the quality of the induced responses. Furthermore, given our interest in non-linear coupling and spectral asymmetries that are characteristic of normal processing, spectra were averaged over subjects to reduce inter-subject variability. This is a form of fixed effects analysis that assumes that every subject can be modeled with the same DCM.

### Model description

The DCM for induced responses is described in [Chen et al. \(2008, 2009, 2010\)](#). In contrast to the DCMs for evoked potentials and cross-spectral densities, the differential equations that underlie this DCM are not based on (Jansen and Rit-like) neural mass models but are simple linear equations similar to the neural state equations used in the DCM for fMRI (but without the hemodynamic responses). They can be expressed as

$$\tau \dot{\vec{g}}(t) = (\underline{A} + v\underline{B})\vec{g}(t) + \vec{u}(t) \quad (1)$$

in which  $\vec{g}(t)$  denotes an  $(J \cdot N)$ -dimensional vector containing spectral power for  $J$  sources and  $N$  frequencies; in our case  $J=2$  and

$N=46$ .  $\tau$  scales the rate of change,  $v$  models condition-dependent effects (see below), and  $\vec{u}(t)$  – a  $(J \cdot N)$ -dimensional vector – specifies the experimental input per source over frequencies.  $\underline{A}$  and  $\underline{B}$  are  $(J \cdot N) \times (J \cdot N)$  matrices that define the coupling across sources and frequencies. To highlight different sources one can express Eq. (1) more explicitly as:

$$\tau \begin{bmatrix} \dot{\vec{g}}_1(t) \\ \vdots \\ \dot{\vec{g}}_J(t) \end{bmatrix} = \left( \begin{bmatrix} \underline{A}_{11} & \dots & \underline{A}_{1J} \\ \vdots & \ddots & \vdots \\ \underline{A}_{J1} & \dots & \underline{A}_{JJ} \end{bmatrix} + v \begin{bmatrix} \underline{B}_{11} & \dots & \underline{B}_{1J} \\ \vdots & \ddots & \vdots \\ \underline{B}_{J1} & \dots & \underline{B}_{JJ} \end{bmatrix} \right) \begin{bmatrix} \vec{g}_1(t) \\ \vdots \\ \vec{g}_J(t) \end{bmatrix} + \begin{bmatrix} \vec{c}_1 \\ \vdots \\ \vec{c}_J \end{bmatrix} u(t) \quad (2)$$

where  $\vec{g}_j$  combines all the spectral power for  $N$  different frequencies at source  $j$ ,  $\vec{c}_j$  specifies how the (now common, hence scalar) external input  $u(t)$  is mapped onto source  $j$ , and  $\underline{A}_{ij}$  and  $\underline{B}_{ij}$  are  $N \times N$  matrices containing cross-frequency coupling parameters between sources  $i$  and  $j$ . Furthermore, one can disambiguate the coupling among frequencies by writing

$$\underline{A}_{ij} = \begin{bmatrix} a_{ij}^{11} & \dots & a_{ij}^{1N} \\ \vdots & \ddots & \vdots \\ a_{ij}^{N1} & \dots & a_{ij}^{NN} \end{bmatrix}. \quad (3)$$

That is, for  $m=n$  the parameter  $a_{ij}^{mn}$  quantifies the iso-frequency coupling between sources  $i$  and  $j$ , and for  $m \neq n$  the cross-frequency coupling. The matrix  $\underline{B}$  specifies condition-dependent changes in coupling strength that are added to the values of  $\underline{A}$ . The experimental design is parameterized using  $v$ ; here  $v=1$  indicates the experimental condition and  $v=0$  stands for the control condition. Finally, the scalar input  $u(t)$  is modeled as a Gaussian bump function at time  $\alpha$  and width  $\beta$ , i.e.  $u(t) = \exp\{-(t-\alpha)^2/2\beta^2\}$ ; here the expected peak occurred around 60 ms after stimulus onset. It has a frequency specific effect for each source  $j$ , i.e.  $\vec{c}_j = [c_j^1, c_j^2, \dots, c_j^N]^T$  which is set to zero ( $\vec{c}_j = \vec{0}$ ) for sources that do not receive exogenous input directly.

The to-be-determined (free) parameters of the model are the scalar values determining the rate of change  $\tau$ , and  $\alpha, \beta$  for the (external) input function, the  $(J \cdot N)$  vector  $\vec{c}$  that further specifies the induced changes by input, as well as the  $(J \cdot N) \times (J \cdot N)$  coupling matrices  $\underline{A}$  and  $\underline{B}$ . For a fully connected model explaining two conditions this may add up to  $2 \cdot (J \cdot N)^2 + (J \cdot N) + 3$  parameters, which, even if the number of sources  $J$  is small, can still be fairly large because of the coupling among  $N$  frequencies. In order to reduce the number of free parameters, we limited the spectral densities to their  $K$  principal modes using singular value decomposition (over all sources and time points). That is, instead of looking at  $J \cdot N$  different time courses of power changes, we considered only  $K$  modes, which in our case (with only one source receiving input) reduced the number of parameters from up to  $2 \cdot (J \cdot N)^2 + (1 \cdot N) + 3 = 2 \cdot (2 \cdot 46)^2 + (1 \cdot 46) + 3 = 16,977$  to  $2 \cdot (J \cdot K)^2 + (1 \cdot K) + 3 = 2 \cdot (2 \cdot 3)^2 + (1 \cdot 3) + 3 = 78$ , when using  $K=3$ .

As such, this DCM allows for a certain class of non-linearities: i.e., ones that are linear in the frequency domain but are necessarily nonlinear in the time domain by virtue of cross-frequency interactions.

### Model specification

Applying DCM to the current data served two purposes: (i) to reveal directional cross-frequency interactions between O and M; and (ii) to identify the alterations in coupling that distinguish trials with fast and slow reaction times. For this, the time–frequency spectra of both trial types should be explained by the same model or neuronal architecture. Recall that the  $\underline{A}$  matrix specifies the connections that

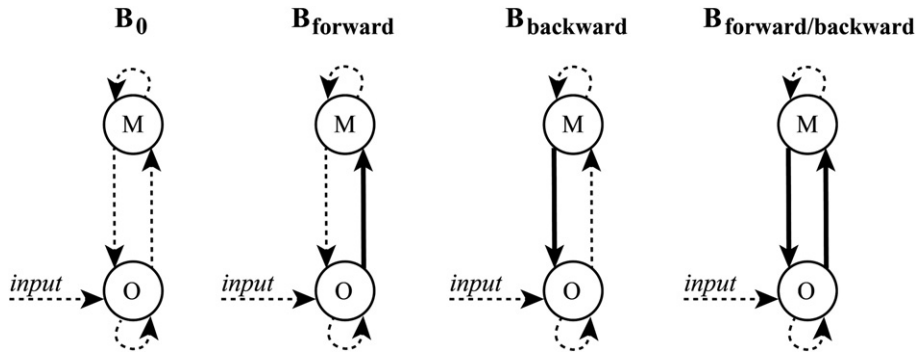


**Fig. 2.** The four model configurations used to explain the data. All contained cross-frequency bidirectional connections, as well as cross-frequency intrinsic connections. The connections that were constrained to have the same coupling strength for both trials with short and long reaction times are indicated by dashed lines, the connections for which condition-dependent modulations were allowed are indicated by solid lines. The models differed only in the  $B$  matrix, respectively allowing for no condition-dependent modulations (model  $B_0$ ), modulations in the forward direction (model  $B_{\text{forward}}$ ), modulations in the backward direction (model  $B_{\text{backward}}$ ), or modulations in both the forward and backward direction (model  $B_{\text{forward/backward}}$ ). Every model was fitted to the data and their performance was compared by means of Bayesian model selection.

are common for both trial types, whereas the  $B$  matrix contains condition-dependent changes in coupling strength, in this case specific to slow reaction times. We compared models that differ in the design matrix  $B$ : no modulations at all (model  $B_0$ ), modulation of the bottom-up (forward) connection between  $O$  and  $M$  (model  $B_{\text{forward}}$ ), modulation of the top-down (backward) connection between  $M$  and  $O$  (model  $B_{\text{backward}}$ ), and modulation of both bottom-up and top-down connections (model  $B_{\text{forward/backward}}$ ); see Fig. 2. We always assumed bidirectional, cross-frequency interactions for the  $A$  matrix. Only  $O$  received external input – mimicking the effect of visual stimulation. The default priors for all parameters are summarized in Table 1. The priors for all self-connections are set to  $-1$  to provide a prior bias towards a stable (linearly damped) system.

#### Parameter fitting

The parameters of a model can, in general, be estimated by various means. Traditionally DCM estimates parameters probabilistically by minimizing the relative entropy defined via data and model outcome. Consider a model of form (1) with a set of parameters  $\theta = \{\tau, \alpha, \beta, \bar{c}, A, B\}$  and the empirical data  $\bar{y}$  to which that model shall be fitted. Then, the corresponding entropy is the relative entropy or Kullback–Leibler divergence between the (approximate) posterior probability density over the parameter values  $\theta$ , i.e.  $p(\theta)$ , and the joint probability density to find both  $\theta$  and  $\bar{y}$ , i.e.  $p(\theta, \bar{y})$ . That is, one minimizes

$$F = KL[p(\theta)||p(\theta, \bar{y})] = \int p(\theta) \log \left[ \frac{p(\theta)}{p(\theta, \bar{y})} \right] d\theta \quad (4)$$

by varying  $p(\theta)$  starting from a prior probability density  $p_0(\theta)$ . Here the generative model is usually expressed in terms of a likelihood and prior probabilities  $p(\theta, \bar{y}) = p(\bar{y}|\theta)p_0(\theta)$ . The Kullback–Leibler divergence in Eq. (4) is also called the variational free energy<sup>1</sup> (e.g., Friston et al., 2006). Minimizing Eq. (4) uses a variational Laplace scheme as described in detail elsewhere; e.g., Friston et al. (2003). The priors are summarized in Table 1.

#### Model comparisons

To select the most likely model generating the observed data, one can determine the log model evidence, which is given by  $\log[p(\bar{y})]$  or its variational free energy approximation:

$$\begin{aligned} F &= - \int p(\theta) \log \left[ \frac{p(\theta|\bar{y})p(\bar{y})}{p(\theta)} \right] d\theta \\ &= - \int p(\theta) \log[p(\bar{y})] d\theta - \int p(\theta) \log \left[ \frac{p(\theta|\bar{y})}{p(\theta)} \right] d\theta \\ &= - \log[p(\bar{y})] + KL(p(\theta)||p(\theta|\bar{y})). \end{aligned} \quad (5)$$

This equation shows that the free energy is an upper bound on the negative log model evidence because the Kullback–Leibler divergence is nonnegative. This means that after optimization of the model parameters, the free energy approaches the negative log model evidence. In other words, the free energy provides an estimate (or at least a lower bound) for the log model evidence and can thus be used for model selection: the model with the smallest free energy (largest log evidence) is the winning model. The significance of the difference between evidences can be obtained by the log-likelihood ratio for two models, i.e.  $F_{\text{model \#1}} - F_{\text{model \#2}}$ . Here we consider the evidence for

**Table 1**

Priors  $p_0(\theta)$  for model parameters  $\theta = \{\tau, \alpha, \beta, \bar{c}, A, B\}$ , where  $p_0(\theta) = p_0(\tau)p_0(\alpha) \dots$

Parameters	Description	Prior density $p_0(\theta) = (\text{mean, variance})$
$\alpha$	Peak latency external input [ms]	$p_0(\alpha) = N(60, 8)$
$\beta = \sqrt{\frac{1}{2} e^{2048/R}}$	Width of Gaussian external input [ms]	$p_0(R) = N(0, \frac{1}{16})$
$\tau = 16 \cdot e^{\kappa}$	Rate constant [ms]	$p_0(\kappa) = N(0, \frac{1}{4})$
$a_{ij}^{mn}$	Internal coupling parameters	$p_0(a_{ij}^{mn}) = \begin{cases} N(0, 1) & \text{for } (n \neq m \text{ and } i \neq j) \\ N(-1, 1) & \text{for } (n = m \text{ and } i = j) \end{cases}$
$b_{ij}^{mn}$	Condition-specific coupling parameters	$p_0(b_{ij}^{mn}) = \begin{cases} N(0, 1) & \text{if present} \\ N(0, 0) & \text{if absent} \end{cases}$
$c_j^n = 32 \cdot \varepsilon_j^n$	External coupling parameters	$p_0(\varepsilon_j^n) = \begin{cases} N(0, \frac{1}{16}) & j = \text{input} \\ N(0, 0) & j \neq \text{input} \end{cases}$

<sup>1</sup> This ‘free energy’ is not to be confused with the conventional term in thermodynamics, defined by Helmholtz and Gibbs in the 19th century.



one model to be strong when this ratio exceeded 3 (which corresponds to a Bayes factor of  $>20$ ).

#### Parameter inference

Once the most likely model – with its configuration of sources and connections – has been selected, the values of its estimated parameters quantify the nature of within- and cross-frequency coupling. As we used frequency modes rather than individual frequencies, the coupling values in  $\underline{A}$  pertain to these modes. To obtain parameter estimates as a function of frequency, we used the projection  $\underline{A}_{ij}(\omega_m, \omega_n) = U \underline{A}_{ij} U^T$ , where  $U$  denotes the orthonormal eigenvector matrix of modes. Similarly for the  $\underline{B}$  matrix.

#### Specific contributions of individual connections

The coupling parameters alone do not provide full insight into the nature of the induced changes in spectral power of the target region.

A strong coupling in combination with only weak input will have limited effect on a target. Conversely, a weak coupling in combination with strong input will have a much larger effect. In order to reveal changes in spectral power induced by a certain connection, we will compare time–frequency spectra generated by the model with and without the connection of interest.

#### Results

The grand-averaged time–frequency spectra of O and M largely resembled the modulations reported by de Lange et al. (2008). After stimulus presentation, a strong gamma band increase emerged in O, quickly followed by a decrease in alpha and beta power in both O and M (see Fig. 3). The first three principal modes collectively explained 95.9% of the original spectral variance and were used for DCM (see Fig. 4A). Visual inspection suggested that all models could produce time–frequency spectra that largely agreed with the observed data (in other words, produced accurate fits). However, the model comparison revealed that  $B_{\text{forward/backward}}$  outperformed the

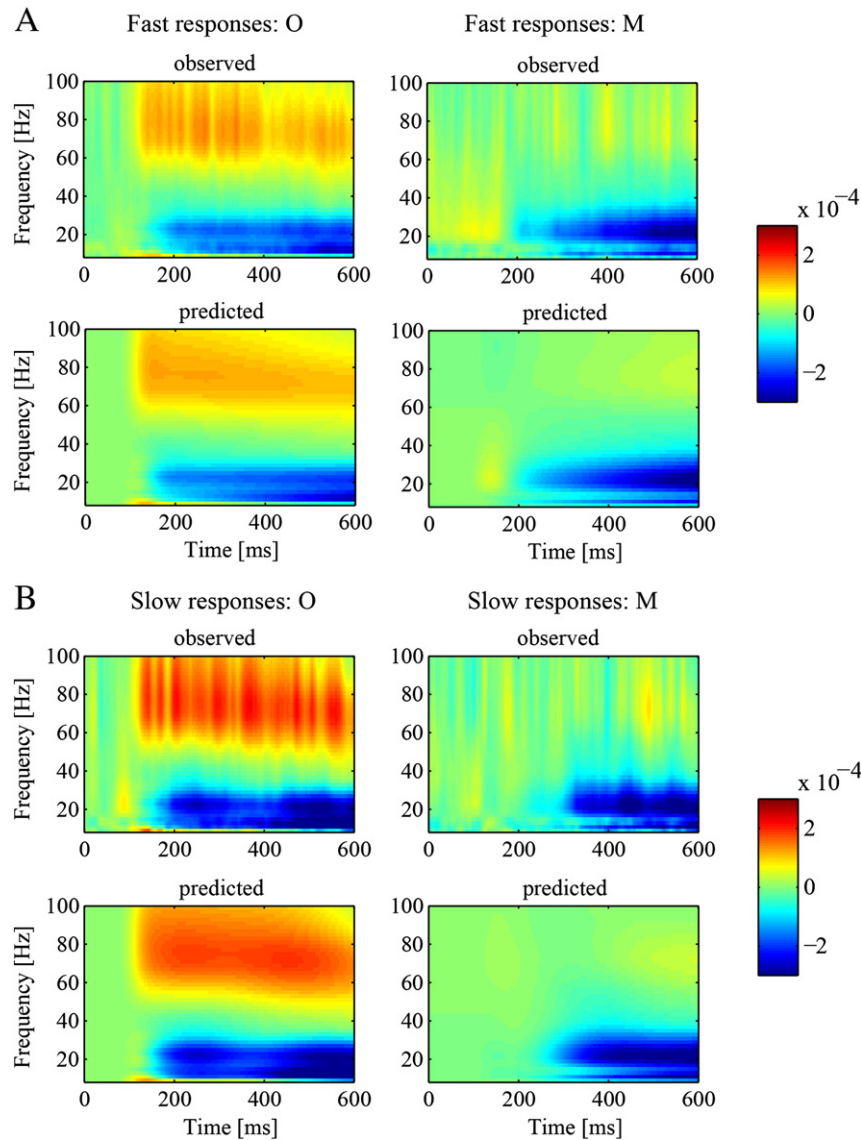


**Fig. 3.** Observed and predicted time–frequency spectra. A) Trials with a short reaction time. B) Trials with a long reaction time. The observed spectra were constructed from the first three frequency modes that collectively explained 95.9% of the original data. The 'predicted' spectra were generated from the winning model  $B_{\text{forward/backward}}$ , which allowed for condition-dependent modulations in both forward (from O to M) and backward (from M to O) direction. As can be seen, a good overall quality of fit was obtained. Note the stronger gamma increase and stronger beta decrease in O for long compared to short reaction time trials.

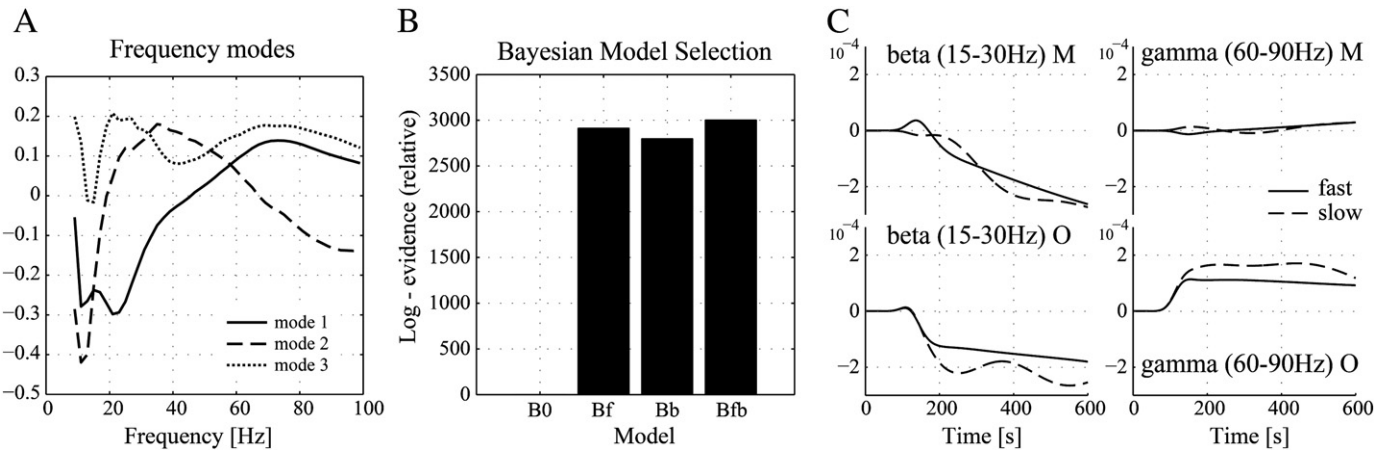


**Fig. 4.** Data characteristics and model comparisons. A) Frequency modes used in the DCM. The modes collectively explained 95.9% variance of the original data: mode 1 (78.7%), mode 2 (14.3%), and mode 3 (2.9%). B) Results of the Bayesian model comparison. The log model evidence of the models is shown with respect to the model with the lowest evidence ( $B_0$ ). The winning model is the one with the largest evidence:  $B_{\text{forward/backward}}$ . The difference with the model that is second best is around 90, which greatly exceeds the value of 3 indicating a significant difference. C) Time courses of modeled spectral power in the beta and gamma band. A stronger beta decrease and gamma increase for fast versus slow reaction time trials can be observed in O. On the contrary, the beta and gamma power in M shows little difference.

other models in terms of model evidence (see Fig. 4B), hence the model in which both the forward connection (from O to M) and the backward (from M to O) connection could differ in strength between trial types represented the data best. Fig. 3 shows that the difference in time–frequency modulations between fast and slow behavioral responses are expressed mainly in O. Trials with longer reaction times induced both a stronger gamma increase and a stronger beta decrease compared to equivalent stimulus processing with shorter reaction times; see also Fig. 4C where the time courses of the average beta and gamma power are depicted.

These results indicate that trials with longer reaction times, and presumably more cognitive effort, are accompanied by altered forward and backward coupling strength between O and M. A simple change in ‘bottom-up’ coupling did not reproduce the data as well, nor did an increase in ‘top-down’ influence from M to O, which might result from a decreased efficiency of motor imagery. It appears that the interaction between O and M leads to a greater gamma increase and beta decrease in O, while the activity patterns in M are relatively preserved. To take a closer look at the contributions of particular connections in generating the time–frequency modulations, we simulated the winning model while selectively removing certain coupling parameters and examined the effects on beta and gamma modulations. The results are summarized in Fig. 5.

The external input to O and its intrinsic dynamics induce the observed gamma increase and beta decrease. Without additional interactions, modulations become stronger over time suggesting that the interaction with M has an attenuating effect. Since our DCM contained only linear differential equations, the contribution of the feedback loop to modulations in O could be inferred by subtracting the effect of external input to O and its intrinsic response from the full time–frequency spectrum of O. This revealed that the gamma increase and beta decrease are counteracted due to the (negative/inhibitory) interaction with M. This holds for both short and long reaction times; with the difference that for long (more difficult) trials this inhibitory effect of the interaction with M is weaker, thereby resulting in a larger gamma increase and beta decrease. Furthermore, the altered forward connection yields an early increase in gamma and decrease in beta, while the altered feedback connection contributes to elevated activity later in time.

The time–frequency modulations in M were weakly affected by the time of the response. This means that, in spite of the different modulations in O, the modulations in M remain unaffected. M does

not receive external input but is fully dependent on input from O and its intrinsic dynamics. Looking at the generated activity when only considering the experimental input to O, the forward connection from O to M and the intrinsic dynamics of O and M, we can observe a decrease in beta power that decays back towards baseline. Completing this model with the backward connection from M to O extends the beta decrease to the end of the epoch. Although the net effect of the  $B$  matrix is small, the induced activity accounted for by the forward and backward connections in isolation for the slow reaction time trials is strongly increased. However, the power decrease caused by the forward connection and the increase caused by the backward connection largely cancel. This is due to the combination of altered activity in O and the changes in connection strengths.

How are these distinct dynamic changes reflected in the cross-frequency components of the couplings? To answer this question we show the coupling matrices  $A$  and  $B$  in Fig. 6. The parameters in these matrices indicate how strong input causes a change in activity in the target region. For example, a positive coupling between power at 10 Hz in O and 20 Hz in M would indicate that increased power in O causes the power in M to rise. Conversely a negative coupling implies that increased power in O has a negative influence on the power in M (either attenuating increased power in M back towards baseline or amplifying decreased power in M). For a large effect, it is crucial that the coupling is strong, and that input activity has a large amplitude. This means that in some cases, large coupling values may have a negligible effect on observed time frequency responses. Therefore the coupling matrices should be interpreted in combination with quantitative time–frequency modulations. The time–frequency modulations for trials with fast responses are generated as follows: the external input induces an increase in alpha, beta and gamma activity in O (not shown). As a consequence of the intrinsic properties of O, the increase in alpha power amplifies the effect of the stimulus. However, for the alpha and beta power there is a strong negative coupling from the beta and gamma band, which ensures that the net effect is a decrease in alpha and beta power. Subsequently, a positive beta to beta coupling between O and M causes the beta power in M to decrease, too. The weak coupling from gamma in O to beta in M only has an attenuating effect. Also the forward connection induces a small drop in gamma power in M early in time. The intrinsic dynamics of M amplify the effect of this small drop by a strong coupling between gamma and beta activity. In addition, there is a negative coupling between frequencies around 40 Hz and the beta

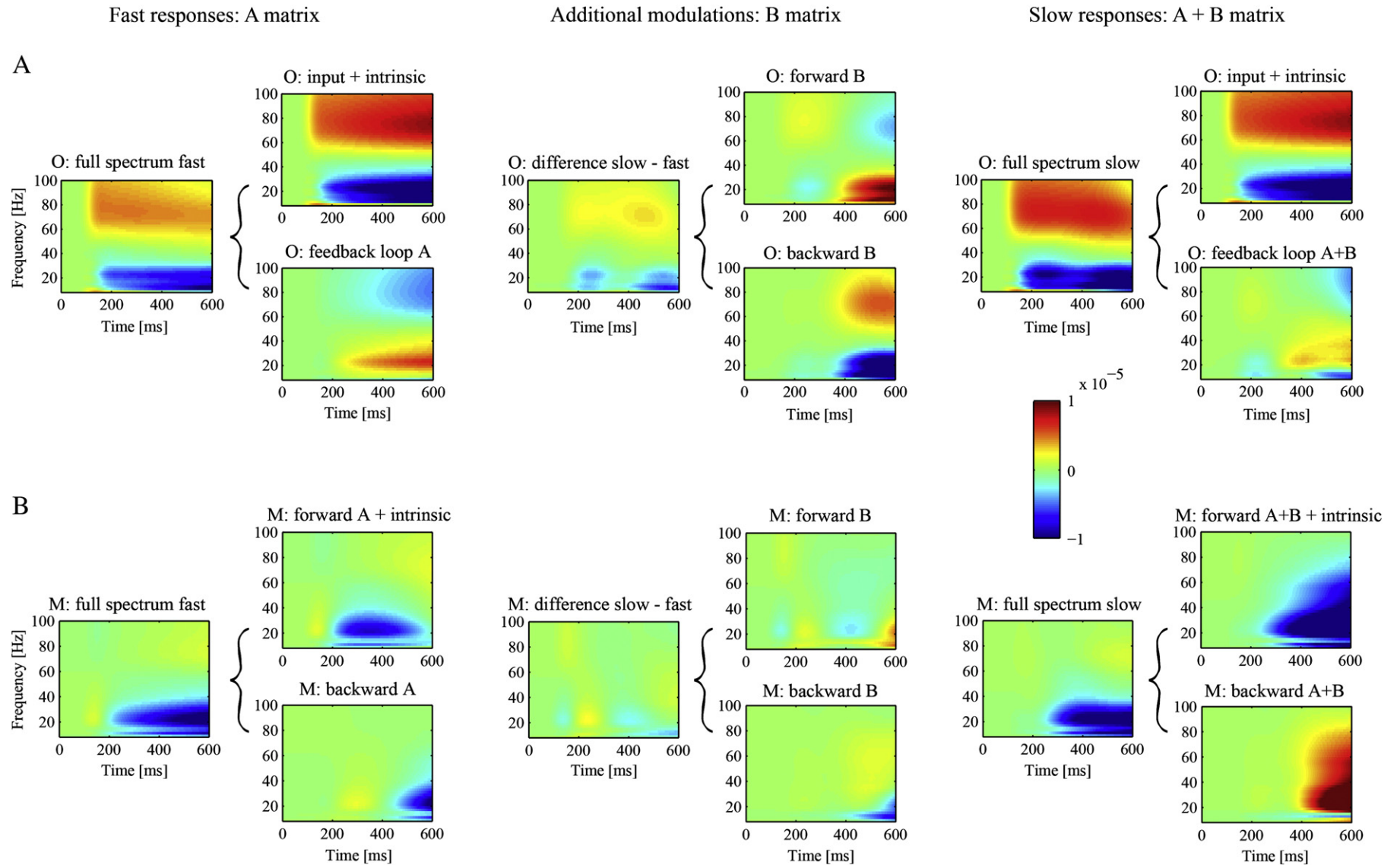


**Fig. 5.** Contributions to the time–frequency spectra by specific connections. A) Modulations in O. B) Modulations in M. The contributions were calculated using simulations of the winning model  $B_{\text{forward/backward}}$  and systematically including or excluding parameters. The linearity of the model allowed for summation or subtraction of predictions to infer the contribution of certain connections. This decomposition was examined for *O: feedback loop A* (*O: full spectrum fast* – *O: input + intrinsic O*); *O: forward B* (*O: input + intrinsic O* + *forward A + B + intrinsic M* + *backward A* – *O: input + intrinsic O* + *forward A + intrinsic M* + *backward A*); *O: backward B* (*O: full spectrum slow* – *O: input + intrinsic O* + *forward A + B + intrinsic M* + *backward A*); *O: feedback loop A + B* (*O: full spectrum slow* – *O: input + intrinsic O*); *M: backward A* (*M: full spectrum fast* – *M: external input + intrinsic O* + *forward A + intrinsic M*); *M: forward B* (*M: input + intrinsic O* + *forward A + B + intrinsic M* + *backward A* – *M: input + intrinsic O* + *forward A + intrinsic M* + *backward A*); *M: backward B* (*M: full spectrum slow* – *M: input + intrinsic O* + *forward A + B + intrinsic M* + *backward A*); *M: backward A + B* (*M: full spectrum slow* – *M: input + intrinsic O* + *forward A + B + intrinsic M*).

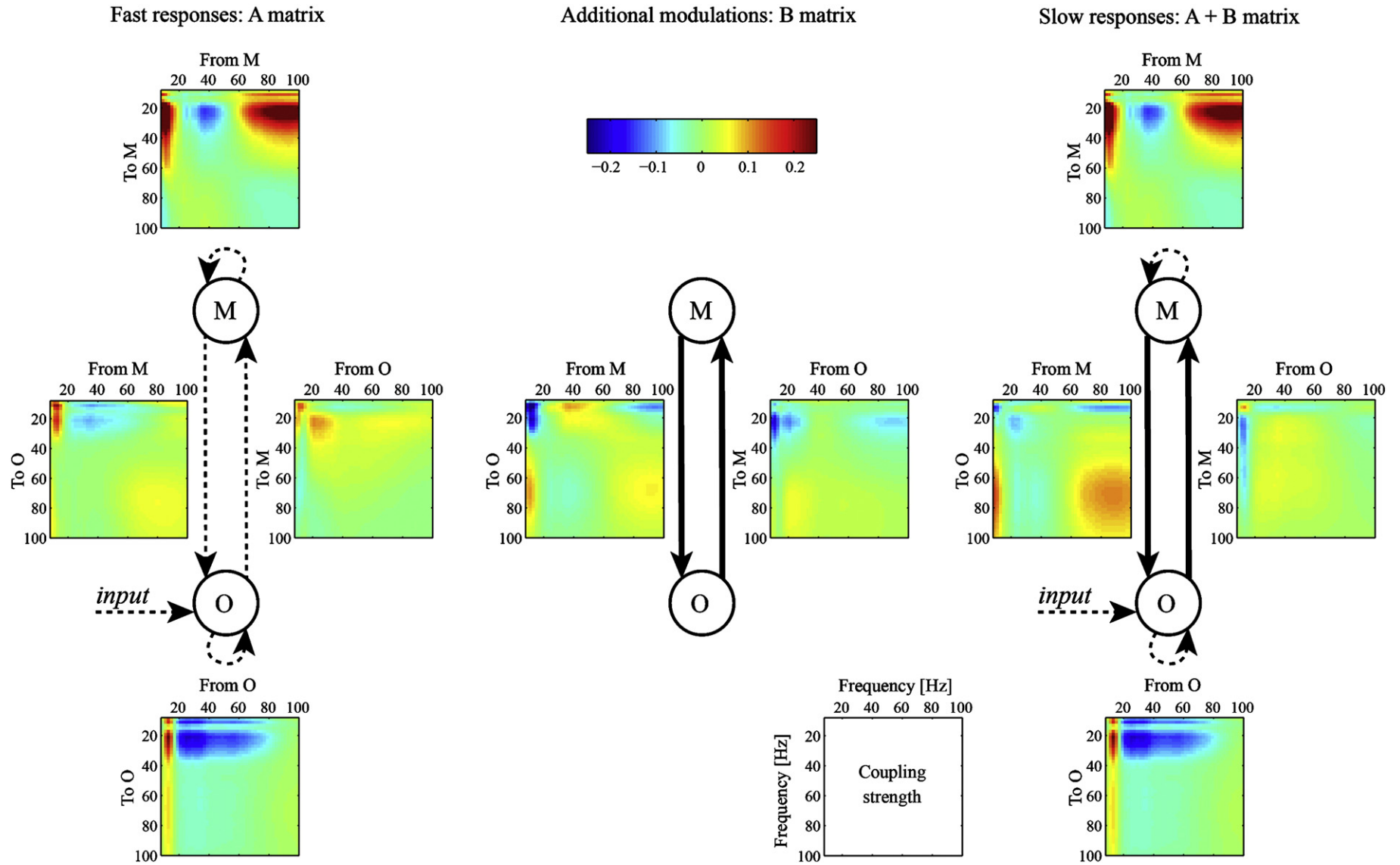


**Fig. 6.** Estimated coupling strengths for all connections. The differential equations of the DCM had the form  $\dot{\vec{x}} = (\vec{A} + \vec{B})\vec{x} + \vec{u}$ , for which the coupling parameters within and between sources for trials with short reaction times are specified in the  $\vec{A}$  matrix. For trials with longer reaction times, condition-dependent changes in coupling strength contained by the  $\vec{B}$  matrix are added to  $\vec{A}$ . Note that the coupling strengths prescribe the rate of change in power of the target source. This means that the influence of a connection should be interpreted in combination with the amplitude of power in the source that acts as an input. A small coupling strength in combination with a large amplitude input may still lead to a substantial change in power in the target source. The contribution of specific cross-frequency couplings to the observed time–frequency spectra are described in more detail in the text.



band. The latter eventually yields a dampening effect of the beta decrease. The positive coupling from alpha to beta seems to somewhat counterbalance this effect. As discussed above, the backward connection from M to O attenuates the gamma increase and beta decrease induced by the stimulus. This is effectuated by the negative beta to gamma coupling. The weak decrease in gamma power in M around 150 ms is positively coupled to the gamma activity in O, which presumably builds up to the large gamma attenuation in O later in time.

Small but important differences in forward and backward coupling underlie the time–frequency spectra for late responses. As can be seen in the middle panel of Fig. 6, there is a small positive beta to gamma coupling in the forward direction. This causes a change in sign of the early gamma modulation in M, which ultimately leads to a reduced attenuating effect of gamma to gamma coupling from M to O. By the same token, a negative beta to gamma coupling from M to O also contributes to higher gamma activity in O. In addition, the reduced gamma to beta coupling in the forward direction leads to a stronger beta decrease in M. However, a weaker negative beta to beta coupling in the backward direction results in a less attenuated beta decrease in O. The feedback loop via O also acts to cancel the excessive power drop induced by the forward connection. Taken together, the intricate interplay between different frequency bands generates the observed time–frequency modulation under different cognitive loads. Small power modulations may have a large influence on activity elsewhere. It is difficult to pinpoint a single cross-frequency interaction as the main mediator.

## Discussion

We used DCM to investigate the mechanisms underlying time–frequency modulations in cortical activity that occurred during the performance of a motor imagery task. Subjects performed a mental rotation of a hand drawing in order to identify it as a left or right hand. The difference between trials with fast and slow behavioral responses was best explained by altered connectivity strength in both the forward and backward direction between O and M. Quantitative details of how the time–frequency spectra had been generated were obtained by selectively studying the corresponding connectivity matrices. The stimulus – jointly with the intrinsic dynamics of O – induced the characteristic gamma increase and beta decrease observed in O. The role of the interaction with M was to attenuate these modulations. The difference between trial types was a weaker attenuating effect in case of slow behavioral responses resulting in stronger modulations in O. Iso-frequency coupling between O and M turned out to be essential for explaining the experimentally observed time–frequency modulations. The beta decrease in O caused a similar decrease in M, while a negative coupling in the reverse direction diminished the beta decrease in O. In turn, the gamma increase in O was attenuated through a gamma to gamma coupling from M. An exception was found for trials with long reaction times, where the beta activity in M caused elevated gamma activity in O.

The largest differences between trial types occurred in O. One could therefore expect that a model for which the intrinsic connection of O is made condition-dependent will outperform the models tested here. Additional analysis, however, showed that this was not the case. Adding the intrinsic coupling of O to the  $B$  matrix of the four models all resulted in significantly lower model evidence than model  $B_{\text{forward/backward}}$ . Nonetheless, there may be other models one could think of to explain the data even better. For instance other configurations of connections in the  $A$  and/or  $B$  matrix or even the use of a different generative model with more complex differential equations. Importantly, the goal of DCM is not to fit the data as accurately as possible but to compare a set of models representing different hypotheses in terms of their evidence; where the evidence reflects both data fit and model complexity. In the present study, we looked at altered coupling between O and M underlying the difference between trials with short and long reaction times. Given the small set

of models we tested here out of all possible models, the largest evidence was obtained for model  $B_{\text{forward/backward}}$ . Likewise, we restricted our analyses to time–frequency modulations in O and M; although more regions have been found to respond during this task using fMRI, including the intraparietal sulcus, occipital-temporal fissure, anterior cingulate sulcus, and a number of frontal regions (de Lange et al., 2005). The parietal source that we additionally found in this data set is likely to mediate the observed interactions between O and M, given the strong resemblance of time–frequency modulations.

The original study by de Lange et al. (2008) has established a correlation between a gamma increase in O and a beta decrease in M. We extend their findings by identifying the directionality of reciprocal cross-frequency coupling between O and M; by explicitly modeling how intrinsic and extrinsic connections mediate the observed time–frequency modulations. Our results suggest that motor imagery, as required during the mental hand rotation task, is not merely a bottom–up process. The reciprocal interaction between occipital and motor areas acts to suppress stimulus-induced activity; therefore, it appears that the top–down connection has an important role in regulating the processing of visual information. In fact, the influence of motor areas on activity in occipital cortex may even co-determine task performance.

Trials with slow behavioral responses presumably required more cognitive effort to perform, reflected in the stronger gamma and beta modulations. This finding is largely in line with the framework of predictive coding (Friston, 2009, 2010; Mumford, 1992; Rao and Ballard, 1999) and the hypothesis that hierarchical levels in the brain operate at different time scales (Kiebel et al., 2008). Conceptually, top–down predictions (slow ‘decision-making’) may be associated with low-frequency oscillations, whereas bottom–up prediction errors (fast ‘input processing’) are broadcast by high-frequency oscillations. In this view, the identification of hand laterality is only completed when gamma levels have decreased sufficiently. Although the coupling from O to M was primarily iso-frequency in the beta band, evidence for a beta to gamma coupling in the top–down direction was found during greater cognitive load on motor imagery. This is sensible in relation to recent work suggesting that superficial layers of visual cortex oscillate at gamma frequencies, while deep layers primarily oscillate at lower frequencies (Buffalo et al., 2011). Since forward connections originate predominantly from superficial layers and backward connections primarily originate in deep layers, these spectral asymmetries suggest that forward connections may use faster (gamma) temporal frequencies, while backward connections may employ lower (alpha or beta) frequencies – a suggestion that has experimental support (Roopun et al., 2010). These asymmetries reflect a necessary synthesis and segregation of forward and backward efferents from afferent input. This segregation can only arise from local nonlinear neuronal computations that are structured and precisely interconnected – nonlinearities that we have characterized quantitatively in this study.

Care should be taken in interpreting the results as a general mechanism for mental rotation in motor imagery. The estimates of coupling strengths turned out to be rather sensitive to small modifications in the experimental data. For example different choices of time and/or frequency intervals could produce large differences in coupling strengths and may even render another model to be the winner. In addition, a number of methodological points complicate the interpretation of results for the DCM used in this study. The closed loop between O and M in our model makes the contributions of individual connections somewhat complicated. Another concern is the use of frequency modes. A single mode often contains more than one frequency peak and hence already captures some of the covariance between frequencies. It is therefore difficult to test for iso-frequency interactions only, even when looking at within-mode coupling. In addition, modes are defined over sources at the same time; however, it might be more

appropriate to perform separate singular value decompositions for each source to capture time frequency responses more completely (in a source specific fashion).

Nevertheless, the use of a generative model might help inferring connectivity patterns from experimental data that may remain concealed with more traditional correlation measures. In this regard, the model(s) used here might be improved by including a neurophysiological foundation like the DCM for evoked potentials (David et al., 2006) and steady-state responses (Moran et al., 2009). This could be important in relation to the recent finding referred to above that neurons in deep layers show synchronization in the alpha band, whereas neurons in superficial layers synchronize their activity in the gamma band (Buffalo et al., 2011), as well as a phase–amplitude coupling between these rhythms within a cortical column (Spaak et al., 2012). Furthermore, the anatomical architecture of cortical columns – giving rise to these layer-specific oscillations – seems to be consistent with the framework of predictive coding (Bastos et al., 2012). Developing models along these lines may be a promising direction of research that could pave the way for identifying directional cross-frequency interactions in a variety of experimental conditions and establishing their synaptic and laminar specific mechanisms.

## Acknowledgments

We thank Floris de Lange for sharing the preprocessed data. This work was financially supported by The Netherlands Organisation for Scientific Research (NWO, grant number 021-002-047) and the Wellcome Trust.

## References

- Bastos, A., Usrey, W.M., Adams, R.A., Mangun, G.R., Fries, P., Friston, K.J., 2012. Canonical microcircuits for predictive coding. *Neuron* 76, 695–711.
- Bruns, A., Eckhorn, R., 2004. Task-related coupling from high- to low-frequency signals among visual cortical areas in human subdural recordings. *Int. J. Psychophysiol.* 51, 97–116.
- Buffalo, E.A., Fries, P., Landman, R., Buschman, T.J., Desimone, R., 2011. Laminar differences in gamma and alpha coherence in the ventral stream. *Proc. Natl. Acad. Sci. U. S. A.* 108, 11262–11267.
- Canolty, R.T., Knight, R.T., 2010. The functional role of cross-frequency coupling. *Trends Cogn. Sci.* 14, 506–515.
- Chen, C.C., Kiebel, S.J., Friston, K.J., 2008. Dynamic causal modelling of induced responses. *Neuroimage* 41, 1293–1312.
- Chen, C.C., Henson, R.N., Stephan, K.E., Kilner, J.M., Friston, K.J., 2009. Forward and backward connections in the brain: a DCM study of functional asymmetries. *Neuroimage* 45, 453–462.
- Chen, C.C., Kilner, J.M., Friston, K.J., Kiebel, S.J., Jolly, R.K., Ward, N.S., 2010. Nonlinear coupling in the human motor system. *J. Neurosci.* 30, 8393–8399.
- David, O., Kiebel, S.J., Harrison, L.M., Mattout, J., Kilner, J.M., Friston, K.J., 2006. Dynamic causal modeling of evoked responses in EEG and MEG. *Neuroimage* 30, 1255–1272.
- de Lange, F.P., Hagoort, P., Toni, I., 2005. Neural topography and content of movement representations. *J. Cogn. Neurosci.* 17, 97–112.
- de Lange, F.P., Jensen, O., Bauer, M., Toni, I., 2008. Interactions between posterior gamma and frontal alpha/beta oscillations during imagined actions. *Front. Hum. Neurosci.* 2, 7.
- Friston, K., 2009. The free-energy principle: a rough guide to the brain? *Trends Cogn. Sci.* 13, 293–301.
- Friston, K., 2010. The free-energy principle: a unified brain theory? *Nat. Rev. Neurosci.* 11, 127–138.
- Friston, K.J., Harrison, L., Penny, W., 2003. Dynamic causal modelling. *Neuroimage* 19, 1273–1302.
- Friston, K., Kilner, J., Harrison, L., 2006. A free energy principle for the brain. *J. Physiol. (Paris)* 100, 70–87.
- Friston, K.J., Bastos, A., Litvak, V., Stephan, K.E., Fries, P., Moran, R.J., 2012. DCM for complex-valued data: cross-spectra, coherence and phase-delays. *Neuroimage* 59, 439–455.
- Hillebrand, A., Barnes, G.R., 2005. Beamformer analysis of MEG data. *Int. Rev. Neurobiol.* 68, 149–171.
- Jansen, B.H., Rit, V.G., 1995. Electroencephalogram and visual-evoked potential generation in a mathematical-model of coupled cortical columns. *Biol. Cybern.* 73, 357–366.
- Jensen, O., Colgin, L.L., 2007. Cross-frequency coupling between neuronal oscillations. *Trends Cogn. Sci.* 11, 267–269.
- Kiebel, S.J., Daunizeau, J., Friston, K.J., 2008. A hierarchy of time-scales and the brain. *PLoS Comput. Biol.* 4, e1000209.
- Litvak, V., Mattout, J., Kiebel, S., Phillips, C., Henson, R., Kilner, J., Barnes, G., Oostenveld, R., Daunizeau, J., Flandin, G., Penny, W., Friston, K., 2011. EEG and MEG data analysis in SPM8. *Comput. Intell. Neurosci.* 2011, 852961.
- Moran, R.J., Stephan, K.E., Seidenbecher, T., Pape, H.C., Dolan, R.J., Friston, K.J., 2009. Dynamic causal models of steady-state responses. *Neuroimage* 44, 796–811.
- Mumford, D., 1992. On the computational architecture of the neocortex. 2. The role of corticocortical loops. *Biol. Cybern.* 66, 241–251.
- Nolte, G., Ziehe, A., Nikulin, V.V., Schlogl, A., Kramer, N., Brismar, T., Muller, K.R., 2008. Robustly estimating the flow direction of information in complex physical systems. *Phys. Rev. Lett.* 100, 234101.
- Penny, W.D., Litvak, V., Fuentemilla, L., Duzel, E., Friston, K., 2009. Dynamic causal models for phase coupling. *J. Neurosci. Methods* 183, 19–30.
- Rao, R.P.N., Ballard, D.H., 1999. Predictive coding in the visual cortex: a functional interpretation of some extra-classical receptive-field effects. *Nat. Neurosci.* 2, 79–87.
- Roopun, A.K., Lebeau, F.E.N., Rammell, J., Cunningham, M.O., Traub, R.D., Whittington, M.A., 2010. Cholinergic neuromodulation controls directed temporal communication in neocortex in vitro. *Front. Neural Circuits* 4, 8.
- Spaak, E., Bonnefond, M., Maier, A., Leopold, D.A., Jensen, O., 2012. Layer-specific entrainment of gamma-band neural activity by the alpha rhythm in monkey visual cortex. *Curr. Biol.* 22, 16.
- Tass, P., Rosenblum, M.G., Weule, J., Kurths, J., Pikovsky, A., Volkman, J., Schnitzler, A., Freund, H.J., 1998. Detection of n:m phase locking from noisy data: application to magnetoencephalography. *Phys. Rev. Lett.* 81, 3291–3294.